Characterization of Saharan dust, marine aerosols and mixtures of biomass-burning aerosols and dust by means of multi-wavelength depolarization and Raman lidar measurements during SAMUM 2

Silke Groß, Matthias Tesche, Volker Freudenthaler, Carlos Toledano, Matthias Wiegner, Albert Ansmann, Dietrich Althausen & Meinhard Seefeldner

TELLUS

Characterization of Saharan dust, marine aerosols and mixtures of biomass-burning aerosols and dust by means of multi-wavelength depolarization and Raman lidar measurements during SAMUM 2

By SILKE GROß[1]*, MATTHIAS TESCHE[2], VOLKER FREUDENTHALER[1], CARLOS TOLEDANO[1,3], MATTHIAS WIEGNER[1], ALBERT ANSMANN[2], DIETRICH ALTHAUSEN[2] and MEINHARD SEEFELDNER[1],   [1]*Meteorological Institute, Ludwig-Maximilians-Universität, Theresienstr. 37, 80333 Munich, Germany;* [2]*Leibniz Institute for Tropospheric Research, Permoserstr. 15, 04318 Leipzig, Germany;* [3]*Group of Atmospheric Optics, Valladolid University, Spain*

ABSTRACT

The particle linear depolarization ratio δ_p of Saharan dust, marine aerosols and mixtures of biomass-burning aerosols from southern West Africa and Saharan dust was determined at three wavelengths with three lidar systems during the SAharan Mineral dUst experiMent 2 at the airport of Praia, Cape Verde, between 22 January and 9 February 2008. The lidar ratio S_p of these major types of tropospheric aerosols was analysed at two wavelengths. For Saharan dust, we find wavelength dependent mean particle linear depolarization ratios δ_p of 0.24–0.27 at 355 nm, 0.29–0.31 at 532 nm and 0.36–0.40 at 710 nm, and wavelength independent mean lidar ratios S_p of 48–70 sr. Mixtures of biomass-burning aerosols and dust show wavelength independent values of δ_p and S_p between 0.12–0.23 and 57–98 sr, respectively. The mean values of marine aerosols range independent of wavelength for δ_p from 0.01 to 0.03 and for S_p from 14 to 24 sr.

1. Introduction

The forth assessment report of the International Panel on Climate Change (IPCC, 2007) pointed out that there are still uncertainties in climate change predictions with respect to climate warming. One reason is the impact of aerosols on the radiative budget (Tegen et al., 1996). As the scattering characteristics of aerosols are very sensitive to their shape, size distribution and composition, these parameters, together with the aerosol vertical distribution, have a strong influence on the radiative impact (Sokolik et al., 2001). Lidar measurements can help to improve our knowledge about aerosols. Already in 1963 Fiocco and Smullin presented a method to detect scattering layers by means of a ruby lidar. Since then the lidar technique underwent a rapid development. With advanced lidar systems it is not only possible to locate scattering layers, but measurements of the extinction and backscatter coefficients at multiple wavelengths allow an estimate of the aerosol's micro-physical parameters (e.g. Müller

et al., 1998; Veselovskii et al., 2002). Because these algorithms are based on Mie theory, they are limited to spherical particles only. In a recent approach, Gasteiger et al. (2011a) introduced a method to derive micro-physical properties of non-spherical particles from lidar measurements, in which the wavelength-dependent particle linear depolarization ratio can be used as additional input parameter.

Lidar depolarization measurements are widely used for aerosol and cloud research (e.g. Sassen, 1991), as they can clearly distinguish spherical particles from non-spherical particles and enable the discrimination of water layers and ice layers in mixed-phase clouds (Ansmann et al., 2005). The volume linear depolarization ratio δ_v was, for example, used to identify volcanic ash in the troposphere and stratosphere (Winker and Osborn, 1992; Sassen et al., 2007), and in another case to distinguish mineral dust from other types of aerosols from space-borne lidar measurements using an empirical threshold for δ_v (Liu et al., 2008a). Most lidar systems employ only one wavelength for the analysis of the particle linear depolarization ratio δ_p of Asian dust (e.g. Chen et al., 2007) and Saharan dust (Liu et al., 2008b). Sugimoto and Lee (2006) showed that using δ_p measurements at two wavelengths helps to distinguish

between different types of aerosol. Model calculations demonstrate that the spectral behaviour of δ_p depends on the size distribution of non-spherical particles (Mishchenko and Sassen, 1998; Wiegner et al., 2009). Measurements of δ_p of mineral dust were performed at four wavelengths over Ouarzazate, Morocco (Freudenthaler et al., 2009), during the first campaign of the SAharan Mineral dUst experiMent (SAMUM; Heintzenberg, 2009).

Mineral dust is a major component of the atmospheric aerosol load, with the strongest source regions in the Saharan desert (Washington et al., 2003). The appearance of Saharan dust plumes strongly depends on time and location (Knippertz et al., 2009, 2011). It is a basic effort to characterize the optical properties of dust at several wavelengths and to separate mineral dust from other types of aerosols to support the modelling of dust transport, to better understand the impact of Saharan dust on the Earth's climate and to provide data to validate and improve radiative transfer codes for non-spherical particles.

Measurements of desert dust over Europe were performed in the framework of the European Aerosol Research Lidar Network (EARLINET; Bösenberg et al., 2003, e.g. Mattis et al., 2002; Ansmann et al., 2003). The observed dust plumes mainly consisted of aged dust, frequently mixed with other types of aerosols. Pure, fresh Saharan dust was investigated during SAMUM 1, 2006, measuring in situ microphysical and chemical properties (e.g. Kaaden et al., 2009; Kandler et al., 2009; Weinzierl et al., 2009), columnar integrated parameters (e.g. Toledano et al., 2009), vertically resolved profiles of dust optical properties (e.g. Esselborn et al., 2009; Freudenthaler et al., 2009; Tesche et al., 2009a), as well as analysing the radiative effects of dust (e.g. Bierwirth et al., 2009). In a resent study, Sakai et al. (2010) showed the differences of the particle linear depolarization ratio δ_p of mineral dust, ammonium sulphate, and sea salt particles, which were measured in a laboratory chamber at 532 nm.

In this work, we present the characterization of the optical properties of Saharan dust by means of lidar measurements at the beginning of its long-range transport over the Atlantic. The investigation includes not only pure desert dust layers, but also mixtures with biomass-burning aerosols from southern West Africa and with marine aerosols. The aerosol layers are classified by means of their particle linear depolarization ratio at three wavelengths (355, 532, and 710 nm), as well as by their lidar ratio determined from Raman measurements at two wavelengths (355 and 532 nm). The measurements were performed during the second campaign of the SAMUM project. A general overview of the measurements performed during SAMUM 2 and their main results are given by Ansmann et al. (2011), and an overview of the general meteorological conditions during SAMUM 2 can be found in Knippertz et al. (2011). In Section 2 the experimental background of our lidar measurements is described. In Section 3 the results are discussed, and Section 4 summarizes this work.

2. Experiment

The aim of the SAharan Mineral dUst experiMent (SAMUM) is to characterize the microphysical, chemical, and optical properties, as well as the vertical distribution of Saharan dust. The first campaign in May and June 2006 was located close to the source regions in Ouarzazate (30.93°N, −6.91°E), Morocco, to measure pure not-aged Saharan dust. The second campaign in January and February 2008 was located at the airport of Praia (75 m asl, 14.948°N, −23.485°E), Cape Verde, on the island Santiago located in the Atlantic Ocean about 700 km west of Senegal. Three lidar systems were located less than 10 m apart from each other and about 1 km from the East coast of the island.

2.1. Instrumentation

The particle linear depolarization ratio δ_p was measured at three wavelengths with three lidar systems: the small, portable, one wavelength POrtable LIdar System (POLIS; Gross et al., 2008) at 355 nm, the MUlti wavelength LIdar System (MULIS; Freudenthaler et al., 2009) at 532 nm, both from the Meteorological Institute of the Ludwig-Maximilians-Universität, München (MIM), and the multi-wavelength system BERTHA (Backscatter Extinction lidar Ratio Temperature Humidity profiling Apparatus; Althausen et al., 2000) from the Institute of Tropospheric Research, Leipzig (IFT), at 710 nm. The range resolution of the raw data of the MIM lidars is 7.5 m, and the temporal average of the raw data is 10 s. The lidar ratios S_p presented in this paper were measured with MULIS at 532 and 355 nm, and with POLIS at 355 nm. POLIS uses a combination of analogue- and photon-counting signals (Whiteman et al., 2006) for data acquisition (LICEL). Although the output power of the laser is only 7 mJ at 20 Hz (355 nm), it is possible to make Raman measurements in the lower to mid-troposphere with this small lidar. Furthermore, the full overlap was reached already at about 100 m range during SAMUM 2, allowing for measurements in the boundary layer, which in general extended up to about 500 m above ground level (agl). Henceforward heights are given agl. The full overlap of MULIS had been adjusted to about 500 m range to better cover the far range, but as MULIS has the possibility of automatic scanning of the lidar pointing in the vertical, it was possible to perform sequential measurements at low (20°) and high (87°) elevation angles in few minutes intervals and to combine the results yielding extinction coefficients, lidar ratios, and depolarization values in the boundary layer also at 532 nm. With BERTHA, measurements at 710 nm were performed with a temporal and spatial resolution of 10 s and 15 m, respectively. The full overlap of BERTHA is reached at 2 km distance from the lidar (Tesche et al., 2009a). However, signals ratios are used in case of depolarization ratio profiling, which causes the overlap effect to widely cancel out and enables measurements down to a height of 300 m. Profiles of the particle linear depolarization ratio were mostly calculated for night-time measurements, for

Table 1. Lidar system parameters

Laser	POLIS Big Sky, Brilliant Ultra	MULIS Continuum, Surelite II	BERTHA Ti:Saphire, Solar TII Ltd. CF 125
Wavelengths (mm)	355	355, 532, 1064	355, 400, 532, 710, 800, 1064
Pulse energy (mJ)	7 (355 nm)	50	20
Repetition rate (Hz)	20	10	30
Beam divergence (mrad)	0.69	0.6	< 0.3
Telescope	Dall-Kirkham	Cassegrain	Cassegrain
Diameter (m)	0.2	0.3	0.53
Focal length (m)	1.2	0.96	3
Field stop (mad)	2.5	0 to 3, adjustable	0.6
Depol.-receiver optics			
Depol.-wavelength (mm)	355	532	710
Interference filter bandwidth (mm)	1.0 FWHM	1.1 FWHM	0.4 FWHM
PBC T_p	0,952	0,983	0.95
PBC R_s	0,999	0,997	0.999
Depol.-calibration methode	$\pm 45°$ mech. rotation	$\pm 45°$ waveplate	$\pm 45°$ polarizer

which the particle backscatter coefficient at 710 nm was derived from the Raman solution at 1064 nm (from signals at 1064 and 607 nm) by using the measured backscatter related 532/1064 nm Ångström exponent (Ångström, 1961). For this retrieval (Tesche et al., 2011), all profiles were smoothed with a window length of 150 m to reduce signal noise. Technical details of the lidar systems can be found in Table 1. Simultaneous lidar measurements of all three lidars were performed from 22 January to 9 February 2008. The typical measurement time was 2 h before noon (morning session) and 3 h after sunset (night session). PO-LIS can either measure in the depolarization or in the Raman mode, the latter only at night. Hence the depolarization measurements were taken during the morning sessions and 2 h before the night sessions, and the Raman measurements during the night sessions.

The sun- and sky-radiometer SSARA (Toledano et al., 2009) from the MIM and a CIMEL CE-318 from the AERONET network (Holben et al., 1998) provide measurements of direct spectral radiances at several wavelengths between 340 and 1550 nm, and scattered radiances from the almucantar geometry (Toledano et al., 2011). Radiosondes were typically launched twice a day at the measurement site, one during the morning session and one during the night session. They provide temperature and pressure profiles for the calibration of the lidar signals in altitudes with clean air (Rayleigh calibration).

2.2. Data evaluation

The analysis of the Raman signals provides independent profiles of the particle extinction coefficient α_p and particle backscatter coefficient β_p, derived from the inelastic N_2-Raman shifted signals at 387 and 607 nm and from the elastic backscattered lidar returns at 355 and 532 nm (Ansmann et al., 1992). The height dependent lidar ratio S_p can then be derived from the ratio of

the particle extinction and backscatter coefficient profiles. Because the signal-to-noise ratio of the Raman channels is quite low, the signals must be averaged over a significant time period, typically 1–2 h. The stability of the atmosphere in such cases was validated by comparing successive lidar profiles of about 1 min average. To further improve the signal-to-noise ratio, the signals are additionally smoothed over range with a sliding average, taking into account that the elastic and inelastic signals are smoothed with the same window length, so that the retrieval of the extinction and backscatter coefficient and consequently the lidar ratio is consistent. Typical smoothing lengths are in the order of a few hundred metres in range. The individual smoothing lengths are reported in Table 2. The smoothing lengths in height are the smoothing lengths in range multiplied by the sine of the elevation angle. The error calculation for the Raman method considers the statistical and systematic error. It is described in detail in Groß et al. (2011b). The relative error of the lidar ratio adds up from the relative errors of the retrievals of the extinction coefficients and of the backscatter coefficients, so that at least moderate aerosol optical depths are required to get sufficiently small errors. In the case studies later and in Tables 3, 4 and A.1, we report these measurement errors together with the mean values.

For the volume linear depolarization ratio δ_v the radiation of the co- ($P_\parallel$) and cross-polarized ($P_\perp$) light with respect to the laser polarization is used, considering a relative calibration factor C between the different channel sensitivities. As for a commercial polarizing beam splitter cube (PBC) the reflectance R_s is usually much better than the transmission T_p, the large co-polarized signal is detected in the reflected branch of the PBC to reduce cross-talk. Polarizing filters behind the PBC additionally suppress cross-talk and consequently reduce the error in the linear depolarization ratio. The calibration factor C includes the transmission of all optics and filters, the diattenuation of the

Table 2. Elevation angles and signal smoothing lengths (range-bins correspond to range, meters to height) used for the analysis of the particle linear depolarization ratio δ_p and of the lidar ratio (Raman) at different height ranges for the three lidar systems

	Date and time (UTC)	Elevation angle	Height (km)	Smooth (rb, m)
POLIS δ_p 355 nm	29 Jan 18:00–20:00	79°	All	11, 81
	30 Jan 18:00–20:00			
	5 Feb 18:00–20:00			
MULIS δ_p 532 nm	29 Jan 19:00–20:00	20°	<0.5	53, 136
	29 Jan 20:40–21:40	87°	>0.5	53, 397
	30 Jan. 20:30–22:30	87°	All	11, 82
	5 Feb 20:45–21:15			
BERTHA δ_p 710 nm	29 Jan 20:40–21:40	90°	All	2, 120
	30 Jan 20:30–22:30			
	5 Feb 20:45–21:15			
POLIS Raman 387 nm	29 Jan 20:50–22:30	79°	<0.3	25, 184
			>0.3	53, 390
	30 Jan 20:30–22:30	79°	<0.5	53, 390
			>0.5	87, 641
	5 Feb 20:45–21:15	78°	<0.5	87, 638
			>0.5	121, 888
MULIS Raman 607 nm	29 Jan 19:00–20:00	20°	<0.5	53, 136
	29 Jan 20:40–21:40	87°	>0.5	53, 397
	30 Jan 20:30–22:30	87°	All	87, 652
	5 Feb 20:45–21:15	20°	<0.5	53, 136
		87°	>0.5	121, 906
MULIS Raman 387 nm	29 Jan 20:40–21:40	20°	<0.5	53, 136
		87°	>0.5	53, 397
	30 Jan 20:30–22:30	87°	All	87, 652
	5 Feb 20:45–21:15	20°	<0.5	53, 136
		87°	>0.5	87, 652

PBC and the electronic amplification of the preamplifiers and photomultipliers.

$$\delta_v = C \frac{p_\perp}{p_\parallel}. \tag{1}$$

It has to be determined from a calibration measurement. The depolarization calibration of all three lidar systems is described in Freudenthaler et al. (2009). All systems employed the high accurate ±45° calibration method. In MULIS, the polarization plane of the incoming light is rotated ±45° by means of a half-wave plate before the PBC, whereas in POLIS the optical receiver behind the receiving telescope is mechanically rotated making use of high-precision mechanical limit stops, and in BERTHA a polarizing sheet filter is inserted before the PBC in ±45° orientations. The particle linear depolarization ratio δ_p is calculated according to Biele et al. (2000)

$$\delta_p = \frac{(1 + \delta_m)\delta_v R - (1 + \delta_v)\delta_m}{(1 + \delta_m)R - (1 + \delta_v)} \tag{2}$$

with the backscatter ratio

$$R = \frac{\beta_m + \beta_p}{\beta_m} \tag{3}$$

and the height-dependent molecular linear depolarization ratio δ_m. The molecular backscatter coefficient β_m is calculated from radio soundings (see e.g. Eberhard, 2010) and the molecular linear depolarization ratio δ_m according to Behrendt and Nakamura (2002). The particle backscatter coefficient β_p is retrieved by means of the Fernald/Klett inversion (Fernald, 1984; Klett, 1985), using a reference value $\beta_p(r_0)$ at a reference range r_0 and the height-dependent lidar ratio S_p from simultaneous or the nearest Raman measurements. In case a Rayleigh calibration around r_0 indicates clean air, the reference value $\beta_p(r_0)$ is assumed to be zero, else $\beta_p(r_0)$ is estimated considering the volume linear depolarization ratio, and the uncertainty of $\beta_p(r_0)$ used for the error calculation is assumed to be $\pm\beta_p(r_0)$. The error analysis is done according to Freudenthaler et al. (2009). In the case studies later and in Tables 3, 4, and A.1 we report these measurement errors together with the mean values.

The lidar ratio S_p and the particle linear depolarization ratio δ_p are intensive parameters of the aerosol and hence only dependent on the aerosol type and independent of the particle number density or signal intensity. For the determination of the mean of the possibly varying intensive parameters over a certain height range or aerosol layer, we weight the values of S_p and δ_p of each

Table 3.   Layer mean values for the case studies of lidar ratio S_p and particle linear depolarization ratio δ_p including systematic errors ($\pm$), the standard deviations of the values within the height range (σ) indicating the variability of the values within the layer, and the retrieved type of aerosol for each lidar system and wavelength. (P355 = POLIS at 355 nm, M355/M532 = MULIS at 355 nm/532 nm, B710 = BERTHA at 710 nm, BBA = biomass burning aerosol.)

Height	S_p	δ_p	Aerosol type
29 January 2008			
0.2–0.4 km	55 ± 3 ($\sigma = 1$) (P355)	0.24 ± 0.02 ($\sigma = 0.005$) (P355)	Saharan dust with few marine aerosols
0.3–0.4 km	51 ± 2 ($\sigma = 1$) (M532)	0.28 ± 0.01 ($\sigma = 0.001$) (M532)	
0.5–0.8 km (δ_p)	60 ± 6 ($\sigma = 3$) (P355)	0.27 ± 0.01 ($\sigma = 0.005$) (P355)	Saharan dust
0.6–0.8 km (S_p)	66 ± 5 ($\sigma = 3$) (M355)	0.30 ± 0.01 ($\sigma = 0.001$) (M532)	
	63 ± 2 ($\sigma = 4$) (M532)	0.36 ± 0.04 ($\sigma = 0.017$) (B710)	
30 January 2008			
0.2–0.5 km	50 ± 2 ($\sigma = 1$) (P355)	0.22 ± 0.01 ($\sigma = 0.005$) (P355)	Saharan dust mixed with marine aerosol
	66 ± 6 ($\sigma = 1$) (M355)	0.29 ± 0.01 ($\sigma = 0.008$) (M532)	
	63 ± 4 ($\sigma = 3$) (M532)	0.36 ± 0.04 ($\sigma = 0.007$) (B710)	
1.6–2.5 km	78 ± 5 ($\sigma = 1$) (P355)	0.17 ± 0.02 ($\sigma = 0.01$) (P355)	BBA
	87 ± 8 ($\sigma = 2$) (M355)	0.16 ± 0.01 ($\sigma = 0.006$) (M532)	
	67 ± 5 ($\sigma = 8$) (M532)	0.18 ± 0.03 ($\sigma = 0.018$) (B710)	
5 February 2008			
0.1–0.3 km	24 ± 6 ($\sigma = 1$) (P355)	0.02 ± 0.01 ($\sigma = 0.01$) (P355)	Marine aerosols
	19 ± 2 ($\sigma = 1$) (M355)	0.02 ± 0.02 ($\sigma = 0.001$) (M532)	
	19 ± 2 ($\sigma = 1$) (M532)		
3.1–3.5	60 ± 4 ($\sigma = 5$) (P355)	0.22 ± 0.02 ($\sigma = 0.07$) (P355)	BBA mixed with Saharan dust
	70 ± 7 ($\sigma = 2$) (M355)	0.18 ± 0.03 ($\sigma = 0.002$) (M532)	
	62 ± 5 ($\sigma = 3$) (M532)	0.19 ± 0.03 ($\sigma = 0.015$) (B710)	
3.8–4.2	63 ± 6 ($\sigma = 4$) (P355)	0.23 ± 0.02 ($\sigma = 0.02$) (P355)	Probably BBA from South America
	64 ± 7 ($\sigma = 3$) (M355)	0.19 ± 0.04 ($\sigma = 0.004$) (M532)	
	86 ± 8 ($\sigma = 3$) (M532)	0.20 ± 0.04 ($\sigma = 0.018$) (B710)	

Table 4.   Summary of the mean particle linear depolarization ratios δ_p and of the mean lidar ratios S_p for the three aerosol types at 532 nm from MULIS measurements and at 355 nm from POLIS measurements ([*]not 5 Feb 1.5–1.9 km)

| Type	Date	δ_p Mean 532 nm	δ_p Range	S_p Mean [sr] 532 nm	S_p range [sr]	δ_p Mean 355 nm	δ_p range	S_p Mean [sr] 355 nm	S_p range [sr]
Dust	26 Jan to 31 Jan and 4 Feb	0.30 ± 0.01	0.29–0.31	62 ± 5	54–70	0.25 ± 0.03	0.24–0.27	58 ± 7	48–63
Dust/BBA	22 Jan to 8 Feb[*]	0.16 ± 0.01	0.12–0.20	69 ± 8	57–84	0.18 ± 0.03	0.15–0.21	75 ± 9	60–98
Marine	4 Feb to 9 Feb	0.02 ± 0.02	0.01–0.02	18 ± 2	17–19	0.02 ± 0.01	0.02–0.03	18 ± 4	14–24

range-bin with the corresponding particle backscatter coefficient for all layer mean values throughout this paper. After the assignment of each aerosol layer to an aerosol type, we calculate the mean values and the standard deviation for each aerosol type, and additionally report the minimum and maximum values for each aerosol type in Table A.1.

3. Observations

The characterization of the vertical aerosol distribution primarily relies on lidar measurements, as they provide height resolved data. This is in particular essential as passive remote sensing instruments like sun photometers and passive satellite sensors cannot resolve several layers of different aerosol types and complex mixtures. In the case studies below we show examples of our analysis of different layering of dust, biomass-burning aerosols and marine aerosols. We use backward trajectories and satellite images to locate possible source regions of the aerosols. The 10 days backward trajectories are calculated with the Hybrid Single Particle Lagrangian Integrated Trajectory model (Draxler and Rolph, 2003; HYSPLIT, 2009) and the NCEP Global Data Assimilation System (GDAS) data in steps of 50 m height levels

Fig. 1. Map of North-West Africa with active dust sources (denoted by letters) during SAMUM-2 detected by visual inspection of the hourly Meteosat Second Generation (MSG) dust RGB composite images (http://oiswww.eumetsat. org/IPPS/html/MSG/RGB/). Overlaid, mainly south of the Sahara, are the colour pixels of the MODIS Burnt Area Product (http://firefly.geog.umd.edu/firemap/) for January 2008. The pixel colours (left scale) indicate the approximate day in January 2008 on which the areas were burnt.
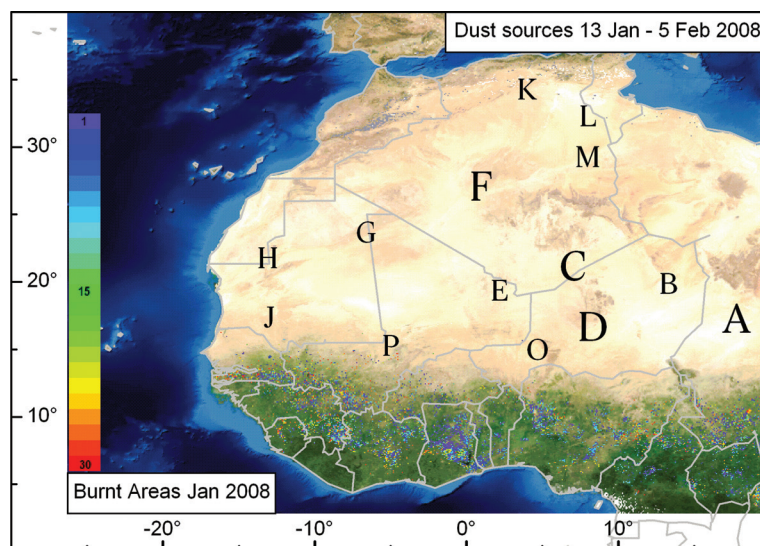
up to 3 km, except for 5 February, where we use 100 m steps up to 5 km. By visual inspection of the hourly dust product images of the Spinning Enhanced Visible and Infrared Imager (SEVIRI) on board of the Meteosat Second Generation satellite (http://oiswww.eumetsat.org/IPPS/html/MSG/RGB/) (see also Knippertz et al., 2011, Figures 7 and 8) we estimated the co-ordinates, time and duration of all dust releases in the relevant region of Northern Africa during the SAMUM 2 period. Figure 1 shows a map of these locations denoted with letters which are larger at generally stronger dust sources. All those dust releases occurred in daytime with maximum activity in the early after-noon, some just for 1 or 2 h, which means that airmasses passing over the source regions in low altitude could only pick up dust during these limited release periods. Also shown on the map in Fig. 1 is the MODIS Burnt Area Product (Justice et al., 2002; Giglio et al., 2006) from the FIRMS (Davis et al., 2009) Web Fire Mapper (http://firefly.geog.umd.edu/firemap/) for January 2008. The burnt areas give a better idea of the amount of burnt biomass than maps showing individual fire hot spots with unde-fined fire strength. As the burnt area pixels are quite scattered and rather isolated, we infer that the biomass burning aerosols in individual lidar signals could stem from some individual fire sources, different for each day, with possibly different aerosol properties. This fact is one of the possible explanations for the variability of the optical properties of biomass burning aerosols. Amraoui et al. (2010) found from Meteosat-8/SEVIRI images that the seasonal fire activities in Africa have a distinct daily cy-cle with a maximum in the early to late afternoon and only few fires at night. Labonne et al. (2007) infered from space-borne Lidar measurements that the buoyancy of the African fires is not sufficient to inject a considerable amount of the biomass burning aerosols into the free troposphere above the mixing layer. We compared the temporally resolved backward trajec-tories with the dust release periods and the fire burning times

considering trajectory heights and local mixing layer heights, and such identified the height levels of the airmasses arriving at Praia which could have picked up dust or biomass burning aerosols. However, subsequent vertical mixing mechanisms not covered by the model can lead to a wider dispersion of the aerosols than evident from this simple investigation. The accu-racy of our aerosol source localization is further influenced by the general uncertainties in trajectory calculations, which are estimated to be typically in the range of 15–20% of the trajec-tory travel distance (Stohl et al., 2002). Ensemble analyses are used to estimate this accuracy in individual cases (e.g. Draxler, 2003). We performed ensemble analyses for all three dates for several characteristic heights, varying the arrival time (± 2 h) and arrival location ($\pm 1°$ longitude and latitude), and found almost the same trajectory patterns for all variations. These analyses indicate that the uncertainties of the trajectory calculations for our three special cases are probably in the lower range of the general uncertainty, and that our aerosol source localizations are good estimates, the better the closer the aerosol sources are in time to the aerosol arrival at the measurement site in Praia. All but one aerosol sources were located 1–5 days before the aerosol arrival in Praia, and within about 1000–5000 km of travel distance.

3.1. Case studies

We present three case studies as examples for the different types of aerosol layering: a pure dust case on 29 January 2008, a case with elevated biomass-burning aerosols above pure dust on 30 January, and a case with biomass-burning aerosols with un-derlying marine boundary layer on 5 February. Figure 2 shows from left to right the particle extinction coefficient α_p at 355 nm as an indication for the amount of aerosol loading, the parti-cle linear depolarization ratios δ_p at 355, 532, and 710 nm, the
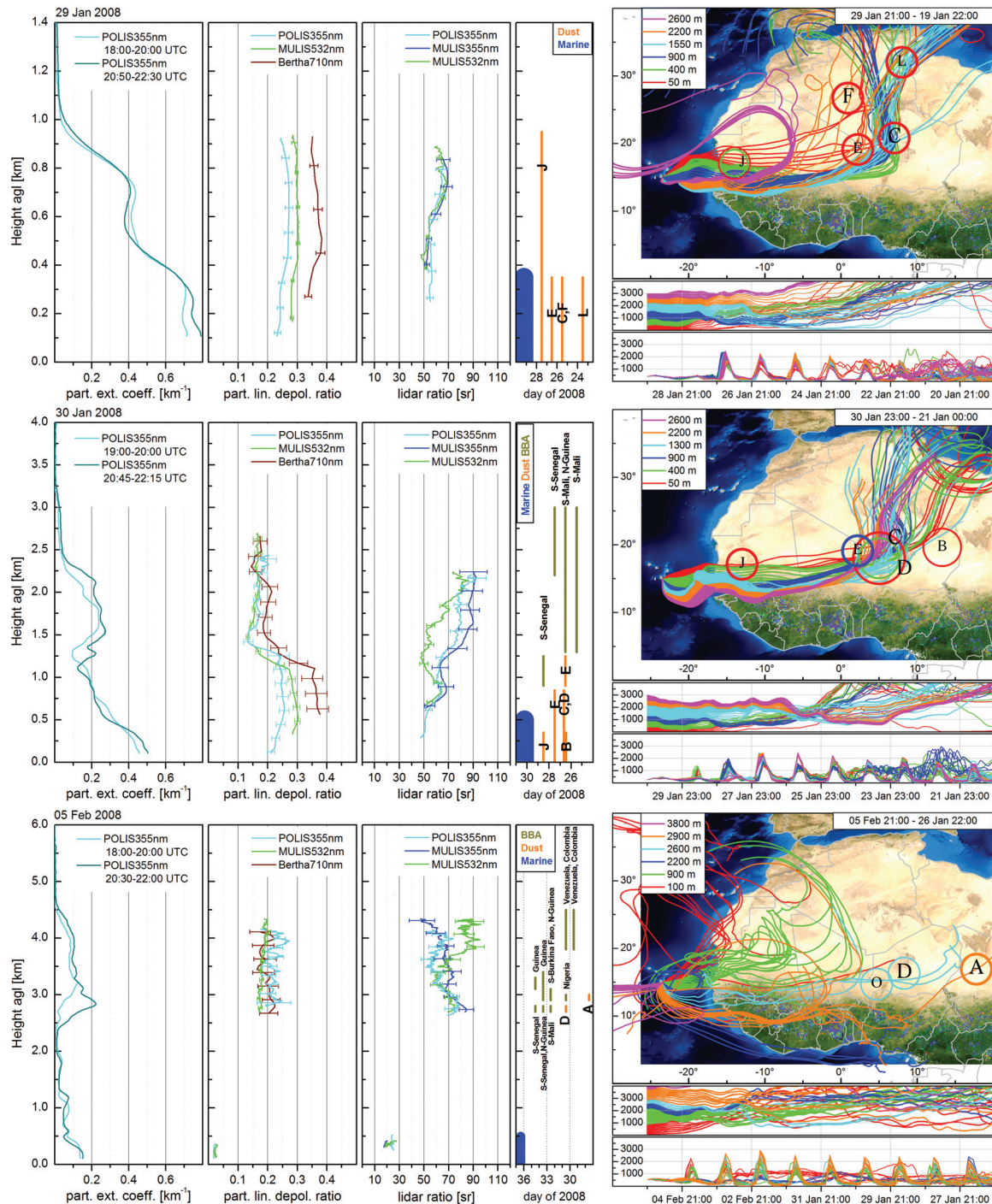
Fig. 2. Profiles of the particle extinction coefficients α_p at 355 nm, of the lidar ratio S_p at 355 and 532 nm, and of the particle linear depolarization ratio δ_p at three wavelengths on 29 and 30 January and 5 February 2008 above Praia. The error bars indicate the systematic uncertainties. Exact times and smoothing lengths are listed in Table 2. The plots at right show the corresponding HYSPLIT backward trajectories (arriving in Praia) on the same map as in Fig. 1. The time periods for the trajectories are given at the top right of the map. The trajectory groups are coloured considering characteristic atmospheric flow patterns. The colour scale shows the colours of the lowermost trajectory of a group. The dust sources (Fig. 1) are encircled with the same colours, indicating their contribution to the dust load to the trajectory group. The graphs below the maps show the heights of the trajectories over time (UTC) and the heights of the mixing layer calculated by HYSPLIT. The plot left of the trajectory map shows the contribution of sources of dust, biomass burning aerosol and marine aerosol to the height ranges of the trajectories arriving in Praia over the date of their uptake into the trajectory group.

lidar ratios S_p at 355 and 532 nm, the heights to which certain dust sources contribute, and the HYSPLIT backward trajectories arriving at Praia on 29 January 21:00 UTC, on 30 January 23:00 UTC and on 5 February 21:00 UTC. The trajectories are grouped and coloured, indicating different spatio-temporal flow patterns which correspond to certain aerosol layers as identified from the lidar measurements. The dust sources, which could have contributed to the aerosol load of certain trajectory groups, are encircled with the corresponding colour, which means: green encircled sources contributed only to the green trajectory group. Shown below the Lat/Lon trajectory plots are the heights of the trajectories and the mixing layer heights over the corresponding period. As explained, POLIS can either measure in Raman or in depolarization mode, and therefore different time periods are used for the determination of the particle linear depolarization ratio of POLIS and of the lidar ratio. The extinction coefficients in Fig. 2 (left) are given for both periods to show that the relevant aerosol layers had been sufficiently persistent, although they sometimes had changed a bit in strength or height. Furthermore, different lidar elevation angles were used and different smoothing lengths applied. These parameters are summarized in Table 2. The extent of the layers and the retrieved mean optical parameters S_p and δ_p of the aerosol layers are summarized in Table 3.

29 January 2008

The first example is for a pure dust case on 29 January (comparable to Knippertz et al., 2011, Fig. 2c), with signal averages from 20:40 to 21:40 UTC (POLIS depolarization measurements 18:00 to 20:00 UTC). Although all trajectories arriving in Praia on 29 January at 21 UTC (see Fig. 2, top-right) passed the Sahara and possible dust sources, only the airmasses arriving below 400 m could have picked up dust from sources L on 23 January, C and F on 25 January, and E on 26 January. Furthermore, marine aerosol could have been mixed in this layer during the last day. Trajectories arriving below about 1 km also passed the dust source J on 27 January within the mixing layer. Clouds prevent to diagnose from the SEVIRI images whether dust had been released on that day, but ground stations in this area reported 'dust raised by the wind' (Knippertz et al., 2011, Figure 8d). Airmasses arriving above about 1 km were not at the right place at the right time to pick up dust or biomass-burning aerosols, or they passed too high above the mixing layer. The lidar signals correspond very well with the trajectory analysis, with aerosol layers (Fig. 2, top-left) reaching to about 1.0 km. The comparison between the 18:00–20:00 UTC and the 20:50–22:30 UTC particle extinction coefficient profiles shows no significant changes in the vertical layering, which allows to use the lidar ratios determined at night for the retrieval of the particle linear depolarization ratio in the evening (for exact times, see Table 2). In the boundary layer up to about 0.4 km, δ_p is wavelength dependent. The retrieved lidar ratios at 355 and 532 nm are not significantly different

considering the systematic errors. Above 0.5 km, the particle linear depolarization ratio also shows a clear wavelength dependence, but with a bit larger δ_p values than in the boundary layer. Like in the boundary layer S_p shows no significant wavelength dependence. They are slightly larger than in the boundary layer. An overview of the retrieved S_p and δ_p is given in Table 3.

30 January 2008

The second example on 30 January 2008 between 20:30 and 22:30 UTC (18:00–20:00 UTC for POLIS depolarization measurements) shows a complex multi-layer structure (Fig. 2, middle). The trajectory analysis shows Saharan dust contributions from sources B–E and J between 26 and 28 January in airmasses arriving in Praia up to about 1.2 km, weak contributions of marine aerosols in the boundary layer up to about 0.5 km from the last day of the travel, and biomass-burning aerosols arriving above about 0.9 km up to about 3 km height stemming from South Senegal, South Mali and North Guinea between 25 and 28 January.

In the boundary layer, δ_p and S_p can only be derived at 355 nm from POLIS measurements. As on 29 January, these values can be assigned to Saharan dust mixed with few marine aerosol and are slightly lower than those in the dust layer between about 0.6 and 1.2 km. In this layer, we see a wavelength dependence of δ_p, whereas S_p is wavelength independent within the error bars. Also the particle extinction coefficient α_p within this layer shows no wavelength dependence. In the second elevated layer above about 1.5 km, α_p as well as S_p show a slight decrease with wavelength. The mean, extinction related Ångström exponent κ is about 1.07 between 355 and 532 nm, indicating small particles. δ_p is wavelength independent. The layer mean values of S_p and δ_p are summarized in Table 3.

5 February 2008

The trajectories arriving in Praia on 5 February 21 UTC show a rather complex situation with strongly changing airflow patterns between adjacent layers, and therefore we do not expect a high accuracy of the trajectories. However, comparing the trajectory analysis with the lidar signals (Fig. 2, bottom), we see a good agreement in the vertical aerosol structure. The airmasses arriving in Praia in the boundary layer and up to about 0.8 km came from North–East and the Atlantic, without direct contact with dust sources. Hence the aerosols in the thin boundary layer up to 0.3 km can be attributed to marine aerosol, which agrees with the meteorological analysis of Knippertz et al. (2011). Although individual trajectories arriving in Praia between about 0.9 and 2.5 km passed some active dust sources between 27 and 31 January, they mostly passed higher than the local mixing layer height probably picking up only few dust, if at all. Consequently, the aerosol load was too low up to about 2.5 km to retrieve

lidar ratios and depolarization values with small enough errors. Airmasses arriving above 2.7–3.5 km collected biomass burning aerosols from the southern West-Africa fire regions between 30 January and 3 February. The 2900 m trajectory additionally passed very low over a strong dust release from source A (Bodele depression) on 27 January. This dust arrived in Praia between the POLIS depolarization measurements in the evening and the lidar ratio measurements in the night. Furthermore, the 2700 and 2800 m trajectories could have picked up dust from source D and O on 30 January. Hence only the heights above 3.1 km, where the extinction coefficient profiles of the evening and night measurements agree well, are used for the further analysis of this elevated aerosol layer. The airmasses above 3800 m came straight from northern South America, leaving the continent in the morning of 3 February and without any subsequent contact with the African continent. Mixing with African airmasses can be excluded, as this trajectory group is clearly detached from the other trajectories. The corresponding Fire and Burnt Area maps (not shown here) show fires in northern Brazil, Venezuela and Colombia.

The analysis of the lidar measurements between 20:30 and 22:00 UTC (POLIS depolarization measurements form 18:00–20:00 UTC) in the boundary layer up to 0.3 km yield no significant wavelength dependence for δ_p and for S_p. Also

in the elevated African biomass burning aerosol layer between 3.1 and 3.5 km no wavelength dependence can be seen in the optical parameters within the error margins. In the South American biomass-burning layer between 3.8 and 4.2 km, the values of δ_p are also wavelength independent, but the mean lidar ratios at 355 and 532 nm show a significant wavelength dependence, in contrast to the lidar ratios of the African biomass-burning aerosols. The layer mean values of δ_p and S_p are summarized in Table 3.

3.2. Layer mean values

The assessment of δ_p and S_p was performed for the whole period between 22 January and 9 February (Fig. 3) in the same way as described in the previous section. In general, we see a structure of three main height ranges during the whole measurement period. The lowest height range, that is the boundary layer which is influenced by convective vertical mixing, extends up to about 0.5 km. The first elevated layers range from about 0.5 to 1.5 km, and the second elevated layers are above about 1.5 km. Averages of δ_p and S_p of aerosol layers in these height ranges, together with their mean systematic error and the standard deviation of the mean over the layer are listed in Table A.1 and plotted in Fig. 3.
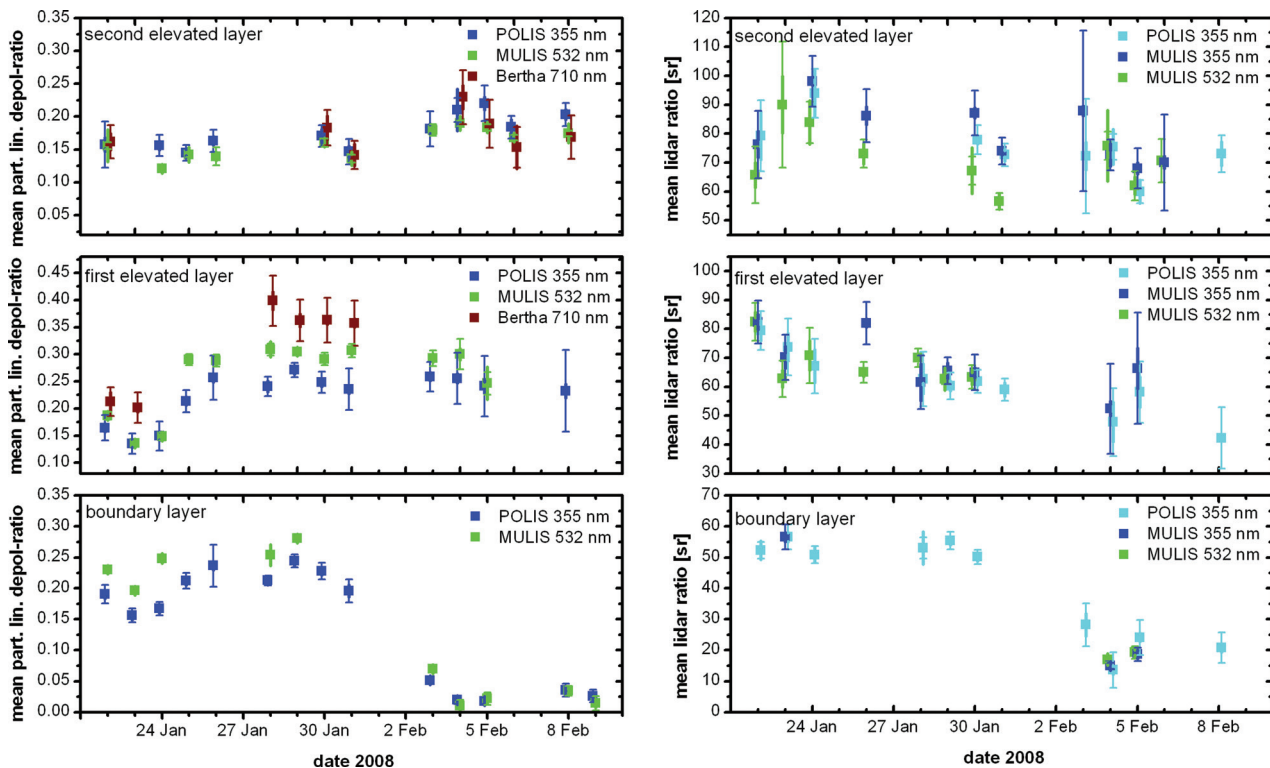
Fig. 3. Backscatter-weighted mean values of the particle linear depolarization ratio at three wavelengths (left) and of the lidar ratio at two wavelengths (right) for different height layers over Praia during SAMUM 2 from Table A.1. The height ranges of the layers had been similar over the whole period, with a boundary layer up to about 0.5 km, and a first and second elevated layer between about 0.5–1.5 km and >1.5 km, respectively. The thick lines show the standard deviation around the mean values, and the error bars show the mean systematic uncertainty.

Knippertz et al. (2011) and Toledano et al. (2011) describe the time periods that exhibit similar features considering the large scale flow pattern and with respect to the source regions of the aerosol measured at Praia. They call these time periods episodes or phases. It is one of our goals to investigate whether or not their discrimination of episodes can also be identified by means of the particle linear depolarization ratio δ_p and the lidar ratio S_p.

During the first episode from 22 to 26 January, S_p is around 54 sr at 355 nm in the boundary layer with corresponding values of $0.16 < \delta_p < 0.25$ for 355 and 532 nm. δ_p shows a weak wavelength dependence with slightly higher values at 532 nm than at 355 nm. Back-trajectories (not shown) indicate the Saharan desert as source region of this aerosols, which subsequently passed over the Atlantic Ocean at low altitudes within the marine boundary layer. Hence these values can probably be attributed to Saharan dust mixed with marine aerosol. The first elevated height layer between about 0.5 and 1.5 km shows wavelength independent mean S_p ranging from 60 to 82 sr and wavelength independent mean δ_p of 0.15 to 0.21. The source region for these airmasses is found to be the Saharan desert, with a very likely influence of the fire regions in southern West Africa. Exceptions from the latter are 25 and 26 January were we find higher mean δ_p values of 0.29 at 532 nm, and 0.21 and 0.26 for 355 nm, maybe due to a larger amount of dust in this layer. The second elevated layer above about 1.5 km shows again high, wavelength independent lidar ratios of 67 sr $< S_p <$ 98 sr and lower δ_p of about 0.15. The back-trajectories clearly indicate southern West Africa as source region. Hence, this height range is probably dominated by biomass burning aerosols in different state of mixing with Saharan dust particles.

During the second period from 27 January to 31 January 2008 we see no differences of mean δ_p and S_p in the boundary layer compared to the first period. The source region of the airmasses can again be located to the Saharan desert with a possible mixing of marine aerosols during the transport over the ocean. In the first elevated layer at about 0.5–1.5 km the mean S_p are wavelength independent between 59 and 70 sr. The mean δ_p values show a clear increase with wavelength with 0.24–0.27 at 355 nm, 0.29–0.31 at 532 nm and 0.36–0.40 at 710 nm. The Saharan desert is clearly identified as source region from backward trajectories, without influence of the biomass burning regions. A quite high overpass over the Atlantic Ocean makes mixing with marine aerosol very unlikely. On 30 and 31 January, an additional second elevated layer is visible above about 1.5 km, with mean S_p again as large as 57–87 sr at 355 and 532 nm, and mean δ_p between 0.14 and 0.18 for all three wavelengths. The back-trajectories indicate southern West Africa as source region for these airmasses, which contain mainly biomass burning aerosol.

For the third episode, from 3 February to 9 February 2008, the airflow pattern in the boundary layer changed to northerly or northeasterly flow (Knippertz et al., 2011) with dominating marine influence. Mean S_p and δ_p in the boundary layer are found to be wavelength independent and quite low with S_p between 15 and 24 sr and δ_p between 0.01 and 0.03. In the first elevated layer between about 0.5 and 1.5 km, we also find wavelength independent values, but as high as 42–80 sr for S_p and 0.23–0.30 for δ_p; however, the errors are large due to low extinction coefficients. In the second elevated layer above about 1.5 km wavelength independent mean S_p and mean δ_p range between 60–87 sr and 0.12–0.23, respectively. The source region allocated to these airmasses is southern West Africa, so again a dominance of biomass burning aerosols with a mixture of Saharan dust is probable for this height range.

3.3. Aerosol classification by means of lidar ratio and particle linear depolarization ratio

Considering the complete time series of δ_p and S_p, plotted in Fig. 3 and listed in Table A.1, we find at 532 nm for transported but pure Saharan dust layer mean values of $0.29 < \delta_p < 0.31$ and 54 sr $< S_p <$ 70 sr, for mixtures of biomass burning aerosols with different amount of dust layer mean values of $0.12 < \delta_p < 0.2$ and 64 sr $< S_p <$ 84 sr and for marine aerosols in the boundary layer $0.01 < \delta_p < 0.02$ and 17 sr $< S_p <$ 19 sr. At 355 nm, we find corresponding layer mean values of $0.24 < \delta_p < 0.27$ and 48 sr $< S_p <$ 63 sr for transported but pure Saharan dust, $0.15 < \delta_p < 0.21$ and 60 sr $< S_p <$ 98 sr for mixtures of biomass burning and dust and $0.02 < \delta_p < 0.03$ and 14 sr $< S_p <$ 24 sr for marine aerosols. At 710 nm, we find δ_p values of $0.36 < \delta_p < 0.40$ for transported but pure Saharan dust, and $0.14 < \delta_p < 0.23$ for mixtures of biomass burning and dust. The mean δ_p and S_p values (considering all measurements) at 355 and 532 nm for the different aerosol types are listed in Table 4. Figure 4 shows for all three wavelength the mean δ_p values and the mean S_p values for 355 and 532 nm. A wavelength dependence of δ_p of Saharan dust is obvious, whereas δ_p of the other considered aerosol types is wavelength independent. S_p shows not wavelength dependence for the considered aerosol types within the error bars.

S_p versus δ_p at 532 nm derived from MULIS measurements and at 355 nm derived from POLIS measurements is plotted in Fig. 5. For this plot only value-pairs from Table A.1 are used for which S_p and δ_p are available from the same lidar, that is at exactly the same measurement conditions. Three different clusters of S_p and δ_p values can be identified: (1) high, wavelength-dependent particle linear depolarization ratios δ_p are correlated with medium, wavelength-independent lidar ratios S_p (Saharan dust); (2) low wavelength-independent δ_p values with low wavelength-independent S_p values (marine aerosols) and (3) medium, wavelength independent δ_p values with high, wavelength-independent S_p values (biomass burning aerosols + dust). Figure 5 shows that it is possible to clearly distinguish the different aerosol types and mixtures of aerosols found during
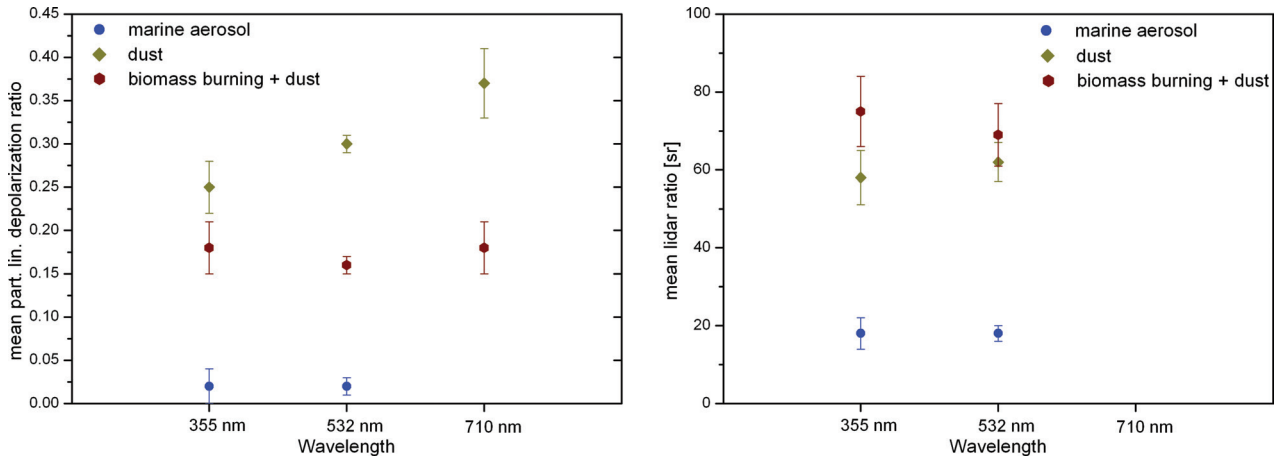
Fig. 4. Mean particle linear depolarization ratio for different aerosol types over wavelength (left) and mean lidar ratio for different aerosol types over wavelength (right). Values assigned to different aerosol types are coloured accordingly. The error bars show the systematic uncertainties of the mean.
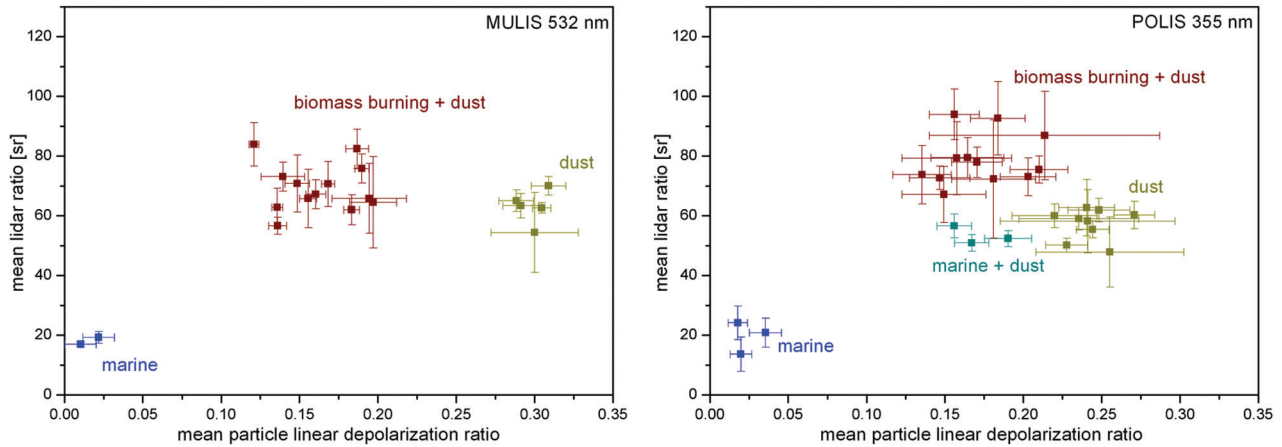

Fig. 5. Mean lidar ratio over mean particle linear depolarization ratio at 532 nm from MULIS measurements (left) and at 355 nm from POLIS measurements (right). Values assigned to different aerosol types are coloured accordingly. The error bars in the horizontal and vertical show the systematic uncertainties of the mean. For this plot only those values from Table A.1 are used, for which both the lidar ratio and the linear depolarization ratio are available from the same lidar system.

SAMUM 2 by means of S_p and δ_p measurements. However, this classification is only possible if the errors of the measurements and of the resultant parameters are well described and small enough.

With accurate measurements, i.e. small errors, it is not only possible to discriminate different aerosol types, but it is also possible to determine the contribution of the individual aerosol components to the total particle extinction coefficient α_p in a two component mixture (e.g. Tesche et al., 2009b).

The total particle extinction coefficient of a two-component mixture is

$$\alpha_p = \alpha_1 + \alpha_2 = (1-x)\alpha_p + x a_p \qquad (4)$$

with α_1 and α_2 being the extinction coefficient of component 1 and component 2, and $x = \alpha_1/\alpha_p$ being the fraction of component 1 to the total particle extinction coefficient. From $S_p = \alpha_p/\beta_p$

follows the lidar ratio of a two-component mixture

$$S_{p,\mathrm{mix}} = \frac{\alpha_1 + \alpha_2}{\dfrac{\alpha_1}{S_{p,1}} + \dfrac{\alpha_2}{S_{p,2}}} = \frac{1}{\dfrac{1-x}{S_{p,1}} + \dfrac{x}{S_{p,2}}} \qquad (5)$$

where $S_{p,1}$ and $S_{p,2}$ are the lidar ratios of the two considered aerosol components in the mixture. Using eq. (11) of the paper published by Gasteiger et al. (2011b), we deduce the particle linear depolarization ratio of a two-component mixture

$$\delta_{p,\mathrm{mix}} = \frac{\dfrac{1-x}{S_{p,1}}\dfrac{\delta_{p,1}}{1+\delta_{p,1}} + \dfrac{x}{S_{p,2}}\dfrac{\delta_{p,2}}{1+\delta_{p,2}}}{\dfrac{1-x}{S_{p,1}}\dfrac{1}{1+\delta_{p,1}} + \dfrac{x}{S_{p,2}}\dfrac{1}{1+\delta_{p,2}}} \qquad (6)$$

with $\delta_{p,1}$ and $\delta_{p,2}$ being the particle linear depolarization ratio of the two considered aerosol components.
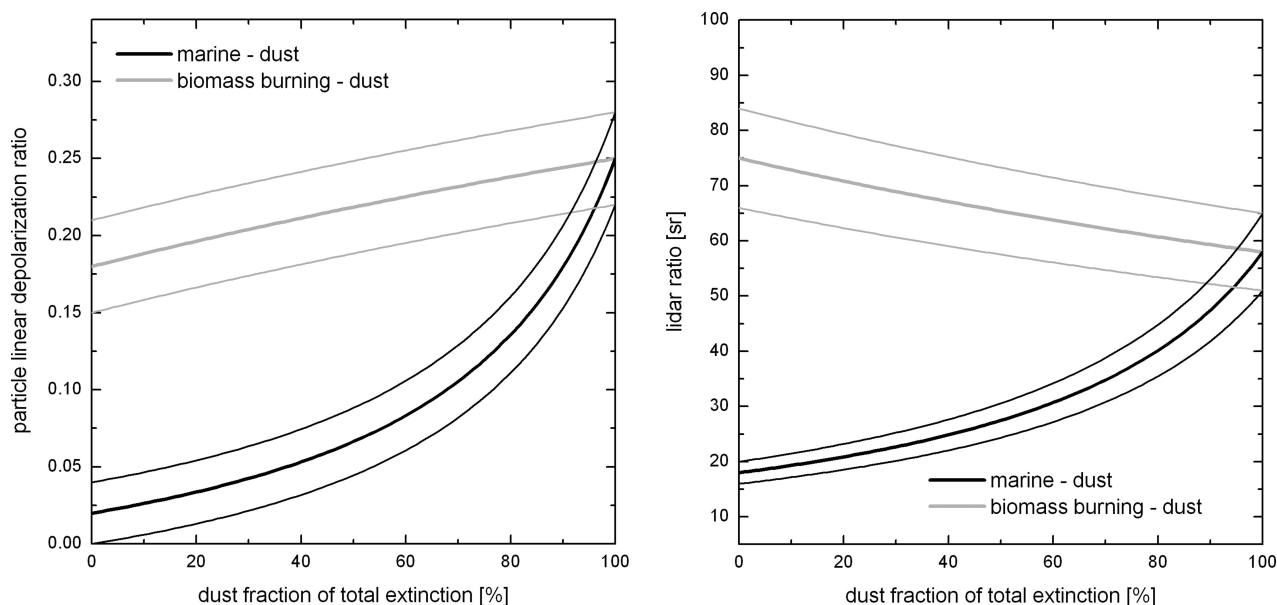
Fig. 6. Particle linear depolarization ratio and lidar ratio over the Saharan dust fraction of the total particle extinction coefficient at 355 nm in a two component mixture of mineral dust and biomass burning aerosols (grey curve), and of a mixture of mineral dust and marine aerosols (black curve). The thick lines show the mean of the retrieval, the thin lines show the maximum and minimum of the retrieval, considering the uncertainties of the input parameters of the pure aerosol components.

Figure 6 shows $\delta_{p,mix}$ and $S_{p,mix}$ over the Saharan dust fraction of α_p for mixtures of Saharan dust and marine aerosols, and for mixtures of Saharan dust and biomass burning aerosols. The measured mean values, listed in Table 4 and shown in Fig. 4, are used as input values ($\delta_{p,1}$ and $\delta_{p,2}$ and $S_{p,1}$ and $S_{p,mix}$) in eqs (5) and (6). The relationship of $\delta_{p,mix}$ and $S_{p,mix}$ to the Saharan dust fraction of α_p is clearly non-linear.

3.4. Discussion of lidar ratio and particle linear depolarization ratio measurements

Most values of the particle linear depolarization ratio δ_p of mineral dust found in the literature are in the range of 0.1–0.25 at 532 nm (e.g. Ansmann et al., 2003; Murayama et al., 2004; Chen et al., 2007), describing long-range transported dust or dust mixed with other types of aerosols. Measurements in fresh dust close to the Taklimakan desert (Iwasaka et al., 2003) or of fresh Gobi dust (e.g. Sakai et al., 2002; Murayama et al., 2004) showed larger values of $0.27 < \delta_p < 0.35$ at 532 nm. Liu et al. (2008b) presented an analysis of space-borne lidar measurements (CALIOP) with mean δ_p values of about 0.32 at 532 nm for a case study of a Saharan dust plume transported over the Atlantic ocean. Measurements at four wavelengths of fresh Saharan dust during SAMUM 1 were presented in Freudenthaler et al. (2009) with mean values of $0.27 < \delta_p < 0.35$ at 532 nm. These δ_p values of fresh Saharan dust are in good agreement with our results for mean δ_p during SAMUM 2 of $0.29 < \delta_p < 0.31$ at 532 nm for the presumptive pure dust layers.

Comparing SAMUM 2 - S_p values of Saharan dust of 48–63 sr at 355 nm and 54–70 sr at 532 nm with the mean values of 55 ± 7 sr at 355 nm and 56 ± 5 sr at 532 nm found during SAMUM 1 (Tesche et al., 2009a), we see a good agreement. These values from measurements are considerably larger than those published by Ackermann (1998), which were calculated using Mie theory for spherical particles. Ackermann found S_p around 42 sr for 355 nm and around 20 sr for 532 nm. These discrepancies highlight that the non-sphericity of particles does not only influence the linear depolarization ratio but also the lidar ratio. Recently Wiegner et al. (2009) and Gasteiger et al. (2011b) presented calculations of the optical parameters of Saharan dust considering the non-sphericity of the particles. Their results are closer to our retrieved values, but significantly depend on the assumed size distribution, on the particle shape and on the real part of the refractive index of dust. The findings of SAMUM 2 will help to improve these calculations.

Measurements of δ_p of marine aerosols and biomass-burning aerosols are rare. Murayama et al. (1999) measured the effect of dust and sea-salt particles in the atmospheric boundary layer and found mean values of $0.01 < \delta_p < 0.10$ at 532 nm. They expected the large values to be connected to dry, crystalline sea-salt particles, or to a mixture of dry sea-salt and dust particles, whereas the lower values were attributed to pure liquid sea-salt particles. Sakai (2000) measured δ_p values of less than 0.05 at 532 nm in airmasses influenced from the Pacific Ocean when the relative humidity was large, and δ_p values larger than 0.1 at low relative humidity (<50%). In a recent study, Sakai et al.

(2010) measured δ_p at 532 nm for sea-salt and NaCl particles in a laboratory chamber and found mean δ_p values of 0.01 for droplets, 0.08 for sea-salt crystals and 0.21 for NaCl crystals. During SAMUM 2, we find wavelength independent δ_p values between 355 and 532 nm of $0.01 < \delta_p < 0.03$ at relative humidity above 50% (see Groß et al., 2011a), which indicates liquid marine aerosols. Mie theory based numerical studies of the lidar ratio S_p of marine aerosols (Ackermann, 1998) result in values between 19 and 27 sr at 355 nm and between 21 and 31 sr at 532 nm for relative humidity above 50%, at which marine aerosols are assumed to be liquid and spherical. Our values of 14 sr $< S_p <$ 24 sr at 355 nm with a mean measurement error of ± 4 sr are a bit smaller but agree within the error bars with the theoretical values, whereas our values of 17 sr $< S_p <$ 19 sr (± 2 sr) at 532 nm are just below the theoretical results.

For the mixture of biomass-burning aerosols in the elevated layers, we find values of $0.12 < \delta_p < 0.23$, wavelength independent for 355, 532 and 710 nm. Heese and Wiegner (2008) reported about particle linear depolarization ratios δ_p of $0.1 < \delta_p < 0.15$ at 355 nm for a mixture of Saharan dust and biomass-burning aerosols measured during the AMMA field campaign. These values are lower than our values during SAMUM 2. For the AMMA data, a high dust load within the mixed layer was assumed, and hence a mean lidar ratio S_p of 55 sr for mineral dust was used for the retrieval of δ_p, which is probably to low, most likely leading to the lower δ_p values. However, Heese and Wiegner (2008) also showed Raman measurements resulting in a mean lidar ratio S_p of 75 ± 15 sr at 355 nm within the mixed layer of dust and biomass burning aerosols. Amiridis et al. (2009) showed a wide range of S_p between 50 and 94 sr at 355 nm for biomass-burning aerosols over Greece that originated from Russian forest fires. Our results of 60–98 sr (mean value 76 sr) for 355 and 532 nm are in good agreement with those values. The high variability of the optical parameters of biomass burning aerosols from our measurements corresponds to the high variability of the particle composition found by Lieke et al. (2011). It can be assumed that the biomass-burning aerosol is not homogenous, but consists of a variety of different burning products and different amounts of desert dust from different sources.

4. Summary

We presented measurements of the particle linear depolarization ratio at three wavelengths and of the lidar ratio at two wavelengths. For this purpose, three ground-based lidar systems were operated. The measurements were performed at Praia, Cape Verde Islands in January and February 2008 during SAMUM 2. Stable multi-layer structures of the atmosphere gave us the opportunity to observe different types of aerosols and aerosol mixtures in well-separated height ranges. In particular, a strong Saharan dust plume provided good conditions to make measurements of transported but pure Saharan dust. Furthermore, marine aerosols and mixtures of dust and biomass burning aerosols originating in the fire regions of southern West Africa are characterized. The particle linear depolarization measurements show mean values of $0.01 < \delta_p < 0.03$ at 355 and 532 nm for marine aerosols, of $0.24 < \delta_p < 0.27$ at 355 nm, $0.29 < \delta_p < 0.31$ at 532 nm and $0.36 < \delta_p < 0.40$ at 710 nm for transported but pure Saharan dust, and of $0.12 < \delta_p < 0.23$ at all three wavelengths for the mixture of dust and biomass burning aerosols. The lidar ratio for these aerosol types are 14–24 sr at 355 nm and 17–19 sr at 532 nm for marine aerosols, 48–63 sr and 54–70 sr for pure transported Saharan dust at 355 and 532 nm, respectively, and of 60–98 sr at both wavelengths for the dust–biomass burning mixture. It is demonstrated that simultaneous measurements of the two intensive properties, that is the particle linear depolarization ratio and the lidar ratio, at two wavelengths allow a classification of the aerosol types, provided that the measurement and retrieval errors are small. The optical properties of pure dust found during SAMUM 1 and SAMUM 2 agree well within the error bars, and hence we see no significantly different influence of the routes of transport from the dust source regions to Morocco and to Cape Verde.

Acknowledgments

Appendix

Table A1. Date and parameters of all measurements of the particle linear depolarization ratio δ_p and of the lidar ratio S_p shown in Fig. 3.

| | | | | Particle linear depolarization ratio δ_p | | | | | | | | Lidar ratio S_p | | | | | |
Date	elev. (°)	from UTC	to UTC	height km	δ_p	$\Delta\delta_p$	$\sigma\delta_p$	max	min	from UTC	to UTC	height km	S_p	ΔS_p	σS_p	max	min
MULIS 532 nm																	
22. Jan	87	16:00	17:00	0.4–0.8	0.23	0.01	0.007	0.25	0.22								
22. Jan	87	16:00	17:00	1.0–1.3	0.19	0.01	0.008	0.20	0.16	20:20	22:30	1.0–1.3	82	7	3	87	71
22. Jan	87	16:00	17:00	1.5–2.5	0.16	0.01	0.024	0.34	0.14	20:20	22:30	2.0–3.0	66	10	4	73	51
23. Jan	87	17:45	18:45	0.4–0.8	0.19	0.01	0.004	0.21	0.18	20:51	22:11						
23. Jan	87	17:45	18:45	1.2–2.0	0.14	0.01	0.003	0.15	0.13	20:51	22:11	1.2–1.7	65	8	3	71	58
24. Jan	87	20:00	22:30	0.3–0.5	0.25	0.01	0.007	0.27	0.22								
24. Jan	87	20:00	22:30	1.1–1.7	0.15	0.01	0.003	0.16	0.14	20:07	22:37	1.1–1.7	71	10	5	80.	56
24. Jan	87	20:00	22:30	2.2–2.9	0.12	0.01	0.006	0.14	0.11	20:07	22:37	2.2–2.9	84	7	8	95	61
26. Jan	87	01:30	02:30	0.5–1.1	0.29	0.01	0.003	0.29	0.28	01:30	02:30	0.8–1.1	60	4	4	67	51
26. Jan	87	01:30	02:30	1.5–2.8	0.14	0.01	0.005	0.16	0.13	01:30	02:30	1.5–2.8	73	5	4	79	64
28. Jan	28	21:10	22:20	0.2–0.4	0.25	0.01	0.016	0.29	0.23								
28. Jan	28	21:10	22:20	0.5–1.2	0.31	0.01	0.014	0.34	0.29	22:44	21:17	0.6–0.8	70	3	5	72	67
29. Jan	29	19:00	20:00	0.2–0.4	0.28	0.01	0.001	0.29	0.28	19:00	20:00	0.3–0.4	51	2	1	52	50
29. Jan	87	20:40	21:40	0.5–0.8	0.30	0.01	0.002	0.31	0.30	21:47	22:18	0.6–0.8	63	2	4	69	54
30. Jan	87	20:35	22:30	0.6–1.2	0.29	0.01	0.008	0.30	0.27	20:35	22:59	0.7–1.0	63	4	3	68	57
30. Jan	87	20:35	22:30	1.6–2.2	0.16	0.01	0.006	0.17	0.14	20:35	22:59	1.6–2.2	67	5	8	85	54
31. Jan	87	20:18	22:16	0.5–1.0	0.31	0.01	0.001	0.31	0.30								
31. Jan	87	20:18	22:16	1.2–4.0	0.14	0.01	0.010	0.17	0.10	20:18	22:16	1.5–1.7	57	3	3	64	53
3. Feb	20	20:30	22:30	0.1–0.2	0.07	0.01	0.002	0.07	0.07								
3. Feb	87	20:30	22:30	0.5–1.0	0.29	0.01	0.003	0.30	0.29								
3. Feb	87	20:30	22:30	1.9–3.0	0.18	0.01	0.004	0.19	0.17								
4. Feb	20	20:00	22:30	0.3–0.4	0.01	0.02	0.001	0.02	0.01	20:05	22:30	0.3–0.4	17	2	2	19	11
4. Feb	87	20:00	22:30	0.8–1.1	0.30	0.03	0.011	0.31	0.26	20:05	22:30	0.8–1.1	54	13	5	65	28
4. Feb	87	20:00	22:30	1.8–2.8	0.19	0.02	0.005	0.21	0.18	20:05	22:30	1.8–2.8	66	12	14	85	38
4. Feb	87	20:00	22:30	3.1–3.9	0.19	0.01	0.010	0.21	0.16	20:05	22:30	3.1–3.9	76	5	12	119	62
5. Feb	20	20:45	21:15	0.2–0.3	0.02	0.02	0.001	0.02	0.03	21:45	23:59	0.2–0.3	19	2	1	24	18
5. Feb	87	20:45	21:15	0.8–1.9	0.25	0.02	0.030	0.29	0.18	21:45	23:45	0.8–1.9	81	19	6	103	57
5. Feb	87	20:45	21:15	3.1–3.5	0.18	0.03	0.002	0.18	0.17	21:45	23:45	3.1–4.5	62	5	3	72	58
5. Feb	87	20:45	21:15	3.8–4.2	0.19	0.04	0.004	0.21	0.18	21:45	23:45	3.8–4.2	86	8	3	95	78
6. Feb	87	20:30	22:30	1.0–2.2	0.20	0.01	0.005	0.21	0.18	20:30	22:30	1.5–2.1	64	15	4	72	51
6. Feb	87	20:30	22:30	3.0–4.5	0.17	0.01	0.006	0.18	0.16	20:30	22:30	3.5–4.5	71	8	9	94	34
8. Feb	20	17:00	19:00	0.2–0.5	0.03	0.02	0.002	0.04	0.03								
8. Feb	87	17:00	19:00	3.6–4.3	0.17	0.01	0.014	0.20	0.04								
9. Feb	20	09:14	09:20	0.1–0.6	0.02	0.01	0.001	0.02	0.01								
POLIS 355 nm																	
22. Jan	80	16:00	17:00	0.1–0.8	0.19	0.02	0.003	0.20	0.18	20:30	22.30	0.2–0.8	52	3	3	57	44
22. Jan	80	16:00	17:00	1.0–1.3	0.16	0.02	0.007	0.18	0.14	20:30	22.30	1.0–1.3	79	7	3	85	71
22. Jan	80	16:00	17:00	1.5–2.0	0.16	0.04	0.010	0.18	0.13	20:30	22.30	2.0–3.0	79	12	8	98	61

Table A1. Continued

		Particle linear depolarization ratio δ_p								Lidar ratio S_p							
	elev. (°)	from UTC	to UTC	height km	δ_p	$\Delta\delta_p$	$\sigma\delta_p$	max	min	from UTC	to UTC	height km	S_p	ΔS_p	σS_p	max	min
23. Jan	80	17:45	18:45	0.2–0.6	0.16	0.01	0.005	0.17	0.15	20:40	22:40	0.2–0.6	57	4	1	60	54
23. Jan	80	17:45	18:45	1.2–2.0	0.14	0.02	0.005	0.15	0.12	20:40	22:40	1.2–1.7	73	10	5	85	66
24. Jan	80	18:00	20:00	0.2–0.5	0.17	0.01	0.005	0.17	0.15	20:30	22:34	0.2–0.5	51	3	2	57	46
24. Jan	80	18:00	20:00	1.1–1.7	0.15	0.03	0.008	0.18	0.14	20:30	22:34	1.1–1.7	67	9	6	81	43
24. Jan	80	18:00	20:00	2.2–2.9	0.16	0.02	0.007	0.19	0.15	20:30	22:34	2.2–2.9	94	8	8	106	68
26. Jan	78.5	02:00	03:00	0.2–0.5	0.24	0.03	0.002	0.24	0.23								
26. Jan	78.5	02:00	03:00	0.5–1.1	0.26	0.04	0.003	0.26	0.25								
26. Jan	78.5	02:00	03:00	1.5–2.8	0.16	0.02	0.007	0.20	0.16								
28. Jan	78	18:30	19:30	0.1–0.4	0.21	0.01	0.005	0.22	0.20	20:50	22:30	0.2–0.4	53	3	5	55	45
28. Jan	78	18:30	19:30	0.5–1.2	0.24	0.02	0.010	0.27	0.22	20:50	22:30	0.6–0.8	63	9	5	73	52
29. Jan	79	18:00	20:00	0.2–0.4	0.24	0.01	0.005	0.26	0.23	20:45	22:15	0.3–0.4	55	3	1	56	53
29. Jan	79	18:00	20:00	0.5–0.8	0.27	0.01	0.005	0.27	0.27	20:45	22:15	0.6–0.8	60	5	1	66	58
30. Jan	79	18:00	20:00	0.1–0.5	0.22	0.01	0.005	0.24	0.21	20:30	22:30	0.2–0.4	50	2	3	51	47
30. Jan	79	18:00	20:00	0.6–1.2	0.25	0.02	0.004	0.26	0.23	20:30	22:30	0.7–1.0	62	4	3	64	58
30. Jan	79	18:00	20:00	1.6–2.2	0.17	0.02	0.010	0.23	0.16	20:30	22:30	1.6–2.2	78	5	2	80	75
31. Jan	79	19:00	19:41	0.1–0.4	0.19	0.02	0.010	0.22	0.18								
31. Jan	79	19:00	19:41	0.5–1.0	0.24	0.03	0.002	0.24	0.23	20:14	22:45	0.5–1.0	59	4	2	65	53
31. Jan	79	17:30	19:30	1.2–2.2	0.15	0.02	0.009	0.20	0.11	20:14	22:45	1.5–1.7	73	4	2	77	74
3. Feb	80	17:30	19:30	0.1–0.3	0.05	0.01	0.001	0.05	0.05	20:20	22:20	0.1–0.3	28	7	4	34	20
3. Feb	80	17:30	19:30	0.7–1.0	0.26	0.03	0.004	0.27	0.23								
3. Feb	80	17:30	19:30	1.9–3.0	0.18	0.03	0.008	0.21	0.15	20:20	22:20	1.9–3.0	72	20	5	86	64
4. Feb	77	15:00	17:00	0.2–0.4	0.02	0.01	0.001	0.02	0.02	21:10	22:20	0.2–0.4	14	6	1	15	11
4. Feb	77	15:00	17:00	0.8–1.1	0.26	0.04	0.009	0.27	0.22	21:10	22:20	0.8–1.1	48	12	7	61	34
4. Feb	77	15:00	17:00	2.4–2.8	0.21	0.07	0.003	0.22	0.21	21:10	22:20	2.4–2.8	87	15	6	102	66
4. Feb	77	15:00	17:00	3.1–3.9	0.21	0.02	0.032	0.25	0.13	21:10	22:20	3.1–3.9	75	5	6	93	60
5. Feb	78	18:00	20:00	0.1–0.3	0.02	0.01	0.01	0.02	0.02	20:30	22:00	0.1–0.3	24	6	1	26	23
5. Feb	78	18:00	20:00	0.8–1.9	0.24	0.06	0.013	0.29	0.21	20:30	22:00	0.8–1.9	58	11	5	75	51
5. Feb	78	18:00	20:00	3.1–3.5	0.22	0.02	0.007	0.24	0.20	20:30	22:00	3.1–3.5	60	4	5	67	51
5. Feb	78	18:00	20:00	3.8–4.2	0.23	0.02	0.020	0.27	0.18	20:30	22:00	3.8–4.2	63	6	4	78	51
6. Feb	78	19:00	19:50	1.5–2.0	0.24	0.05	0.006	0.25	0.23								
6. Feb	77	19:00	19:50	3.5–4.5	0.18	0.02	0.012	0.21	0.15								
8. Feb	79	18:00	20:00	0.2–0.5	0.03	0.01	0.001	0.04	0.03	20:30	22:30	0.2–0.5	21	5	1	24	16
8. Feb	79	18:00	20:00	1.0–1.3	0.23	0.08	0.013	0.26	0.20	20:30	22:30	1.0–1.3	42	11	7	60	27
8. Feb	79	18:00	20:00	3.6–4.3	0.20	0.02	0.008	0.22	0.18	20:30	22:30	3.6–4.3	73	6	4	86	61
9. Feb	76	09:00	09:45	0.1–0.6	0.03	0.01	0.001	0.03	0.02								
BERTHA 710 nm																	
22. Jan	90	20:05	22:31	0.4–0.8	0.27	0.03	0.009	0.28	0.26								
22. Jan	90	20:05	22:31	1.0–1.3	0.21	0.03	0.016	0.23	0.19								
22. Jan	90	20:05	22:31	1.5–2.0	0.16	0.03	0.013	0.19	0.14								
23. Jan	90	20:51	22:10	0.4–0.8	0.28	0.03	0.008	0.30	0.27								
23. Jan	90	20:51	22:10	1.2–1.9	0.20	0.03	0.004	0.21	0.19								

Table A1. Continued

		Particle linear depolarization ratio δ_p								Lidar ratio S_p							
	elev. (°)	from UTC	to UTC	height km	δ_p	$\Delta\delta_p$	$\sigma\delta_p$	max	min	from UTC	to UTC	height km	S_p	ΔS_p	σS_p	max	min
28. Jan	90	21:10	22:20	0.5–1.2	0.40	0.05	0.017	0.44	0.34								
29. Jan	90	20:40	21:40	0.5–0.8	0.36	0.04	0.017	0.38	0.34								
30. Jan	90	20:08	22:58	0.6–1.0	0.36	0.04	0.007	0.38	0.35								
30. Jan	90	20:08	22:58	1.6–2.5	0.18	0.03	0.018	0.21	0.14								
31. Jan	90	21:32	23:32	0.5–1.5	0.36	0.04	0.004	0.36	0.35								
31. Jan	90	21:32	23:32	1.5–4.0	0.14	0.02	0.017	0.19	0.11								
4. Feb	90	21:21	22:14	1.7–2.9	0.23	0.04	0.018	0.26	0.19								
4. Feb	90	21:21	22:14	3.1–3.9	0.23	0.04	0.016	0.26	0.19								
5. Feb	90	20:45	21:15	3.1–3.5	0.19	0.03	0.015	0.21	0.16								
5. Feb	90	20:45	21:15	3.8–4.1	0.20	0.04	0.018	0.22	0.17								
6. Feb	90	20:49	22:35	3.5–4.0	0.15	0.03	0.032	0.19	0.05								
MULIS 355 nm																	
22. Jan	87									20:20	22:30	1.0–1.3	82	7	3	86	75
22. Jan	87									20:20	22:30	2.0–3.0	76	11	5	84	65
23. Jan	87									20:51	22:11	0.4–0.8	57	4	2	59	54
23. Jan	87									20:51	22:11	1.2–1.7	74	10	5	85	66
24. Jan	87									20:07	22:37	1.1–1.7	81	13	2	86	73
24. Jan	87									20:07	22:37	2.2–2.9	98	9	1	102	91
26. Jan	87									01:30	02:30	0.8–1.1	82	7	1	84	79
26. Jan	87									01:30	02:30	1.5–2.8	86	9	3	91	80
28. Jan	28									22:44	21:17	0.6–0.8	65	8	3	68	59
29. Jan	87									21:47	22:18	0.6–0.8	66	5	3	69	59
30. Jan	87									20:35	22:59	0.7–1.0	66	6	1	68	59
30. Jan	87									20:35	22:59	1.6–2.2	87	8	2	90	82
31. Jan	87									20:18	22:16	1.5–1.7	74	5	1	76	71
4. Feb	20									20:05	22:30	0.3–0.4	15	1	1	16	12
4. Feb	87									20:05	22:30	0.8–1.1	52	16	3	47	57
4. Feb	87									20:05	22:30	1.8–2.8	75	15	9	56	87
4. Feb	87									20:05	22:30	3.1–3.9	73	5	4	64	80
5. Feb	20									21:45	23:59	0.2–0.3	19	2	1	24	17
5. Feb	87									21:45	23:45	0.8–1.9	66	19	7	85	58
5. Feb	87									21:45	23:45	3.1–3.5	70	7	2	74	67
5. Feb	87									21:45	23:45	3.8–4.2	64	7	3	69	56
6. Feb	87									20:30	22:30	1.5–2.1	70	17	2	78	63
6. Feb	87									20:30	22:30	3.5–4.5	79	10	4	89	70

Elev. denotes the lidar pointing elevation angle from horizontal, σ and min/max denote the standard deviations and the minimum and maximum values within the height range, Δ denotes the systematic errors ($\pm$).

References

Ackermann, J. 1998. The extinction-to-backscatter ratio of tropospheric aerosol: a numerical study. *J. Atmos. Oceanic Technol.*, **15**, 1043–1050, doi:10.1175/1520-0426.

Althausen, D., Müller, D., Ansmann, A., Wandinger, U., Hube, H. and co-authors. 2000. Scanning 6–wavelength 11–channel aerosol lidar. *J. Atmos. Oceanic Technol*, **17**, 1469–1482.

Amiridis, V., Balis, D. S., Giannakaki, E., Stohl, A., Kazadzis, S. and co-authors. 2009. Optical characteristics of biomass burning aerosols over Southeastern Europe determined from UV-Raman lidar measurements. *Atmos. Chem. Phys.*, **9**, 2431–2440, doi:10.5194/acp-9-2431-2009.

Amraoui, M., DaCamara, C. C. and Pereira, J. M. C. 2010. Detection and monitoring of African vegetation fires using MSG-SEVIRI imagery. *Remote Sens. Environ.*, **114**, 1038–1052, doi:10.1016/j.rse.2009.12.019.

Ångström, A. 1961. Techniques of determining the turbidity of the atmosphere. *Tellus* **13**, 214–223.

Ansmann, A., Wandinger, U., Riebesell, M., Weitkamp, C. and Michaelis, W. 1992. Independent measurement of extinction and backscatter profiles in cirrus clouds by using a combined Raman elastic-backscatter lidar. *Appl. Opt.*, **31**, 7113, doi:10.1364/AO.31.007113.

Ansmann, A., Bösenberg, J., Chaikovsky, A., Comerón, A., Eckhardt, S. and co-authors 2003. Long-range transport of Saharan dust to northern Europe: The 11–16 October 2001 outbreak observed with EARLINET. *J. Geophys. Res.* **108**, doi:10.1029/2003JD003757.

Ansmann, A., Mattis, I., Müller, D., Wandinger, U., Radlach, M. and co-authors 2005. Ice formation in Saharan dust over central Europe observed with temperature/humidity/aerosol Raman lidar. *J. Geophys. Res.* **110**, doi:10.1029/2005JD005000.

Ansmann, A., Petzold, A., Kandler, K., Tegen, I., Wendisch, M. and co-authors. 2011. Saharan mineral dust experiments SAMUM-1 and SAMUM-2: what have we learned? *Tellus* **63B**, this issue.

Behrendt, A. and Nakamura., T. 2002. Calculation of the calibration constant of polarization lidar and its dependency on atmospheric temperature. *Opt. Exp.* **10**, 805–817.

Biele, J., Beyerle, G. and Baumgarten G. 2000. Polarization lidar: corrections of instrumental effects. *Opt. Exp.* **7**, 427–435.

Bierwirth, E., Wendisch, M., Ehrlich, A., Heese, B., Tesche, M. and co-authors. 2009. Spectral surface albedo over Morocco and its impact on radiative forcing of Saharan dust. *Tellus* **61B**(1), 252–269, doi:10.1111/j.1600–0889.2008.00395.x

Bösenberg, J., Ansmann, A., Baldasano, J. M., Balis, D., Böckmann, C. and co-authors. 2003. EARLINET: A European Aerosol Research Lidar Network to Establish an Aerosol Climatology, Max-Planck-Institut Report, **348**, Hamburg.

Chen, W.-N., Tsai, F.-J., Chou, C. C. K., Chang, S.-Y., Chen, Y.-W. and co-authors. 2007. Optical properties of Asian dusts in the free atmosphere measured by Raman lidar at Taipei, Taiwan. *Atmos. Environ.*, **41**(36), 7698–7714, doi:10.1016/j.atmosenv.2007.06.001.

Davies, D. K., Ilavajhala, S., Wong, M. M. and Justice, C. O. 2009. Fire information for resource management system: archiving and distributing MODIS active fire data. *IEEE Trans. Geosci. Remote Sens.*, **47**, 72–79.

Draxler, R. R. 2003: Evaluation of an ensemble dispersion calculation. *J. Appl. Meteor.*, **42**, 308–317, doi: 10.1175/1520-0450(2003)042<0308:EOAEDC>2.0.CO;2.

Draxler, R. R. and Rolph, G. D. 2003. *HYSPLIT (HYbrid Single Particle Lagrangian Integrated Trajectory) Model, Air Resour. Lab.*, NOAA, Silver Spring, MD. Available at: http://ready.arl.noaa.gov/HYSPLIT.php.

Eberhard, W. L. 2010. Correct equations and common approximations for calculating Rayleigh scatter in pure gases and mixtures and evaluation of differences. *Appl. Opt.* **49**, 1116–1130.

Esselborn, M., Wirth, M., Fix, A., Weinzierl, B., Rasp, K. and co-authors. 2009. Spatial distribution and optical properties of Saharan dust observed by airborne high spectral resolution lidar during SAMUM 2006. *Tellus* **B61**, 131–143, doi:10.1111/j.1600-0889.2008.00394.x.

Fernald, F. G. 1984. Analysis of atmospheric lidar observations: some comments. *Appl. Opt.* **23**, 652–653.

Fiocco, G. and Smullin, L. D. 1963. Detection of scattering layers in the upper atmosphere (60–140 km) by optical radar. *Nature* **199**, 1275–1276, doi:10.1038/1991275a0.

Freudenthaler, V., Esselborn, M., Wiegner, M., Heese, B., Tesche, M. and co-authors. 2009. Depolarization ratio profiling at several wavelengths in pure Saharan dust during SAMUM 2006. *Tellus* **61B**, 165–179, doi:10.1111/j.1600–0889.2008.00396.x.

Gasteiger, J., Groß, S., Freudenthaler, V. and Wiegner, M. 2011a. Volcanic ash from Iceland over Munich: mass concentration retrieved from ground-based remote sensing measurements. *Atmos. Chem. Phys.*, **11**, 2209–2223, doi:10.5194/acp-11-2209-2011.

Gasteiger, J., Wiegner, M., Groß, S., Freudenthaler, V., Toledano, C. and co-authors. 2011b. Modeling lidar-relevant optical properties of complex mineral dust aerosols. *Tellus* **63B**, this issue.

Giglio, L., van der Werf, G. R., Randerson, J. T., Collatz, G. J. and Kasibhatla, P. 2006. Global estimation of burned area using MODIS active fire observations. *Atmos. Chem. Phys.*, **6**, 957–974.

Groß, S., Freudenthaler, V., Toledano, C., Seefeldner, M. and Wiegner, M. 2008. Mini-lidar measurements of particle depolarization and Raman scattering of Saharan-dust and biomass burning at 355 nm during SAMUM 2, In: *Proceedings of 24th International Laser Radar Conference, Boulder, USA*, 23–27 June 2008, S04P-10.

Groß, S., Gasteiger, J., Freudenthaler, V., Wiegner, M., Geiß, A. and co-authors. 2011a. Characterization of the planetary boundary layer during SAMUM-2 by means of lidar measurements. *Tellus* **63B**, this issue.

Groß, S., Wiegner, M., Freudenthaler, V. and Toledano, C. 2011b. Lidar ratio of Saharan dust over Cape Verde Islands: Assessment and error calculation, *J. Geophys. Res.*, doi:10.1029/2010JD015435, in press.

Heese, B. and Wiegner, M. 2008. Vertical aerosol profiles from Raman polarization lidar observations during the dry season AMMA field campaign. *J. Geophys. Res.*, **113**, D00C11+, doi:10.1029/2007JD009487.

Heintzenberg, J. 2009. The SAMUM-1 experiment over Southern Morocco: overview and introduction. *Tellus*, **61B**, 2–11.

Holben, B., Eck, T. F., Slutsker, I., Tanré, D., Buis, J. P. and co-authors. 1998. AERONET—a federated instrument network and data archive for aerosol characterization. *Remote Sens. Environ.*, **66**, 1–16, doi:10.1016/S0034-427(98)00031-5.

HYSPLIT Dispersion Model Website, 2009, *Air Resources Laboratory, National Oceanic and Atmospheric Administration*. Available at: http://www.arl.noaa.gov/ready/hysplit4.html.

Iwasaka, Y., Shibata, T., Nagatani, T., Shi, G.-Y., Kim, Y. S. and co-authors. 2003. Large depolarization ratio of free tropospheric aerosols over the Taklamakan desert revealed by lidar measurements: possible diffusion and transport of dust particles. *J. Geophys. Res.*, **108**, doi:10.1029/2002JD003267.

IPCC, Climat change. 2007. *The Physical Science Basis*. Cambridge University Press, Cambridge.

Justice, C. O., Giglio, L., Korontzi, S., Owens, J., Morisette, J. T. and co-authors. 2002. The MODIS fire products. *Remote Sens. Environ.*, **83**, 244–262.

Kaaden, N., Massling, A., Schladitz, A., Müller, T., Kandler, K. and co-authors. 2009. State of mixing, shape factor, number size distribution, and hygroscopic growth of the Saharan anthropogenic and mineral dust aerosol at Tinfou, Morocco. *Tellus*, **61B**, 51–63, doi:10.1111/j.1600-0889.2008.00388.x.

Kandler, K., Schütz, L., Deutscher, C., Ebert, M., Hofmann, H. and co-authors. 2009. Size distribution, mass concentration, chemical and mineralogical composition and derived optical parameters of the boundary layer aerosol at Tinfou, Morocco, during SAMUM 2006. *Tellus*, **61B**, 32–50, doi:10.1111/j.1600-0889.2008.00385.x.

Klett, J. D. 1985. Lidar inversion with variable backscatter/extinction ratios. *Appl. Opt.* **24**, 1638–1643.

Knippertz, P, Ansmann, A., Althausen, D., Müller, D., Tesche, M. and co-authors. 2009, Dust mobilization and transport in the northern Sahara during SAMUM 2006—a meteorological overview. *Tellus*, **61B**, 12–31, doi:10.1111/j.1600-0889.2008.00380.x.

Knippertz, P., Tesche, M., Heinold, B., Kandler, K., Toledano, C. and co-authors. 2011. Dust mobilization and transport from West Africa to Cape Verde—a meteorological overview of SAMUM–2. *Tellus* **63B**, this issue.

Labonne, M., Bréon, F.-M. and Chevallier, F. 2007. Injection height of biomass burning aerosols as seen from a spaceborne lidar. *Geophys. Res. Lett.*, **34**, doi: 10.1029/2007GL029311.

Lieke, K., Kandler, K., Scheuvens, D., Emmel, C., von Glahn, C. and co-authors. 2011. Particle chemical properties in the vertical column based on aircraft observations in the vicinity of Cape Verde islands. *Tellus* **63B**, this issue.

Liu, Z., Liu, D., Huang, J., Vaughan, M., Uno, I. and co-authors. 2008a. Airborne dust distributions over the Tibetan Plateau and surrounding areas derived from the first year of calipso lidar observations. *Atmos. Chem. Phys.*, **8**, 5045–5060.

Liu, Z., Omar, A., Vaughan, M., Hair, J., Kittaka, C. and co-authors. 2008b. Calipso lidar observations of the optical properties of Saharan dust: A case study of long-range transport. *J. Geophys. Res.*, **113**, D07207+, doi:10.1029/2007JD008878.

Mattis, I., Ansmann, A., Müller, D., Wandinger, U. and Althausen, D. 2002. Dual-wavelength Raman lidar observations of the extinction-to-backscatter ratio of Saharan dust. *Geophys. Res. Lett.*, **29**, 1306+, doi:10.1029/2002GL014721.

Mishchenko, M. I. and Sassen, K. 1998. Depolarization of lidar returns by small ice crystals: an application to contrails. *Geophys. Res. Lett.* **25**, 309–312.

Müller, D., Wandinger, U., Althausen, D., Mattis, I. and Ansmann, A. 1998. Retrieval of physical particle properties from lidar observations

of extinction and backscatter at multiple wavelengths. *Appl. Opt.*, **37**, 2260–2263, doi:10.1364/AO.37.002260.

Murayama, T., Okamoto, H., Kaneyasu, N., Kamataki, H. and Miura, K. 1999. Application of lidar depolarization measurement in the atmospheric boundary layer: Effects of dust and sea-salt particles. *J. Geophys. Res.*, **104**, null-31792, doi:10.1029/1999JD900503.

Murayama, T., Müller, D., Wada, K., Shimizu, A., Sekiguchi, M. and co-authors. 2004. Characterization of Asian dust and Siberian smoke with multiwavelength Raman lidar over Tokyo, Japan in spring 2003. *Geophys. Res. Lett.* **31**, doi:10.1029/2004GL021105.

Sakai, T. 2000. Free tropospheric aerosol backscatter, depolarization ratio, and relative humidity measured with the Raman lidar at Nagoya in 1994–1997: contributions of aerosols from the Asian continent and the Pacific Ocean. *Atmos. Environ.*, **34**, 431–442, doi:10.1016/S1352–2310(99)00328-3.

Sakai, T., Shibata, T., Iwasaka, Y., Nagai, T., Nakazato, M. and co-authors. 2002. Case study of Raman lidar measurements of Asian dust events in 2000 and 2001 at Nagoya and Tsukuba, Japan. *Atmos. Environ.*, **36**, 5479–5489, doi:10.1016/S1352–2310(02)00664-7.

Sakai, T., Nagai, T., Zaizen, Y. and Mano, Y. 2010. Backscattering linear depolarization ratio measurements of mineral, sea-salt, and ammonium sulfate particles simulated in a laboratory chamber. *Appl. Opt.*, **49**, 4441–4449, doi:10.1364/AO.49.004441.

Sassen, K. 1991. The polarization lidar technique for cloud research: a review and current assessment. *Bull. Am. Meteorol. Soc.*, **72**, 1848–1866.

Sassen, K., Zhu, J., Webley, P., Dean, K. and Cobb, P. 2007. Volcanic ash plume identification using polarization lidar: Augustine eruption, Alaska. *Geophys. Res. Lett.*, **34**, L08803+, doi:10.1029/2006GL027237.

Sokolik, I. N., Winker, D. M., Bergametti, G., Gillette, D. A., Carmichael, G. and co-authors. 2001. Introduction to special section: outstanding problems in quantifying the radiative impacts of mineral dust. *Geophys. Res. Lett.*, **106**, 015–018.

Stohl, A., Eckhardt, S., Forster, C., James, P., Spichtinger, N. and co-authors. 2002. A replacement for simple back trajectory calculations in the interpretation of atmospheric trace substance measurements. *Atmos. Environ.*, **36**, 4635 − 4648.

Sugimoto, N. and Lee, C. H. 2006. Characteristics of dust aerosols inferred from lidar depolarization measurements at two wavelengths. *Appl. Opt.*, **45**, 7468–7474.

Tegen, I., Lacis, A. A. and Fung, I. 1996. The influence on climate forcing of mineral aerosols from disturbed soils. *Nature*, **380**, 419–422.

Tesche, M., Ansmann, A., Müller, D., Althausen, D., Mattis, I. and co-authors. 2009a. Vertical profiling of Saharan dust with Raman lidars and airborne HSRL in southern Morocco during samum. *Tellus* **61B**, 144–164 doi:10.1111/j.1600-0889.2008.00390.x

Tesche., M., Ansmann, A., Müller, D., Althausen, D., Engelmann, R. and co-authors. 2009b. Vertically resolved separation of dust and smoke over Cape Verde by using mulitwavelength Raman and polarization lidars during Saharan Mineral Dust Experiment 2008. *J. Geophys. Res.* **114**, doi: 10.1029/2009JD011862.

Tesche, M., Groß, S., Ansmann, A., Müller, D., Althausen, D. and co-authors. 2011, Profiling of Saharan dust and biomass burning smoke with multiwavelength polarization Raman lidar at Cape Verde. *Tellus* **63B**, this issue.

Toledano, C., Wiegner, M., Garhammer, M., Seefeldner, M., Freuden-
thaler, V. and co-authors. 2009. Spectral aerosol optical depth charac-
terization of desert dust during SAMUM 2006. *Tellus* **61B**, 216–228,
doi:10.1111/j.1600-0889.2008.00382.x.

Toledano, C., Wiegner, M., Groß, S., Freudenthaler, V., Gasteiger, J. and
co-authors. 2011. Optical properties of aerosol mixtures derived from
sun-sky radiometer during SAMUM-2, *Tellus* **63B**, this issue.

Veselovskii, I., Kolgotin, A., Griaznov, V., Müller, D., Wandinger, U.
and co-authors. 2002. Inversion with regularization for the retrieval of
tropospheric aerosol parameters from multiwavelength lidar sound-
ing. *Appl. Opt.*, **41**, 3685–3699.

Washington, R., Todd, M., Middleton, N. J. and Goudie, A. S. 2003.
Dust-storm source areas determined by the total ozone monitoring
spectrometer and surface observations. *Ann. Assoc. Am. Geograph.*,
93, 297–313.

Weinzierl, B., Petzold, A., Esselborn, M., Wirth, M., Rasp, K. and co-
authors. 2009. Airborne measurements of dust layer properties, parti-
cle size distribution and mixing state of Saharan dust during samum
2006. *Tellus*, **61B**, 96–117, doi:10.1111/j.1600-0889.2008.00392.x

Whiteman, D. N., Demoz, B., Rush, K., Schwemmer, G., Gentry, B. and
co-authors. 2006. Raman lidar measurements during the international
h2o project. Part I: Instrumentation and analysis techniques. *J. Atmos.
Oceanic Technol.*, **23**, 157–169, doi:10.1175/JTECH1838.1.

Wiegner, M., Gasteiger, J., Kandler, K., Weinzierl, B., Rasp, K. and co-
authors. 2009. Numerical simulations of optical properties of Saharan
dust aerosols with special emphasis on the linear depolarization ratio.
Tellus **61B**. 180–194, doi:10.1111/j.1600-0889.2008.00381.x.

Winker, D. M. and Osborn, M. T. 1992. Airborne lidar observa-
tions of the Pinatubo volcanic plume. *Geophys. Res. Lett.*, **19**,
doi:10.1029/91GL02867.